

# Deep Learning Reconstruction for 9-View Dual Energy CT Baggage Scanner

Yoseob Han  
KAIST, Daejeon, Korea  
Email: hanyoseob@kaist.ac.kr

Jingu Kang  
GEMSS Medical Co. Seongnam, Korea  
Email: jingu.kang@gemss-medical.com

Jong Chul Ye  
KAIST, Daejeon, Korea  
Email: jong.ye@kaist.ac.kr

**Abstract**—For homeland and transportation security applications, 2D X-ray explosive detection system (EDS) have been widely used, but they have limitations in recognizing 3D shape of the hidden objects. Among various types of 3D computed tomography (CT) systems to address this issue, this paper is interested in a stationary CT using fixed X-ray sources and detectors. However, due to the limited number of projection views, analytic reconstruction algorithms produce severe streaking artifacts. Inspired by recent success of deep learning approach for sparse view CT reconstruction, here we propose a novel image and sinogram domain deep learning architecture for 3D reconstruction from very sparse view measurement. The algorithm has been tested with the real data from a prototype 9-view dual energy stationary CT EDS carry-on baggage scanner developed by GEMSS Medical Systems, Korea, which confirms the superior reconstruction performance over the existing approaches.

**Index terms**— Explosive detection system (EDS), sparse-view X-ray CT, convolutional neural network (CNN)

## I. INTRODUCTION

In homeland and aviation security applications, there has been increasing demand for X-ray CT EDS system for carry-on baggage screening. A CT-EDS can produce an accurate 3D object structure for segmentation and threat detection, which is often not possible when a 2D-EDS system captures projection views in only one or two angular directions. There are currently two types of CT EDS systems: gantry-based CT and stationary CT. While gantry-based CT EDS is largely the same as medical CT, baggage screening should be carried out continuously, so it is often difficult to continuously screen carry-on bags because of the possible mechanical overloading of the gantry system. On the other hand, a stationary CT EDS system uses fixed X-ray sources and detectors, making the system suitable for routine carry-on baggage inspection.

For example, Fig. 1 shows source and detector geometry of the prototype stationary CT-EDS system developed by GEMSS Medical Systems, Korea. As shown in Fig. 1(a), nine pairs of X-ray source and dual energy detector in the opposite direction are distributed at the same angular interval. For seamless screening without stopping conveyer belt, each pair of source and detectors are arranged along the  $z$ -direction as shown in Fig. 1(b) so that different projection view data can be collected while the carry-on baggages moves continuously on the conveyor belt. Then, 9-view fan beam projection data is obtained for each  $z$ -slice by rebinning the measurement data. This type of stationary CT system is suitable for EDS

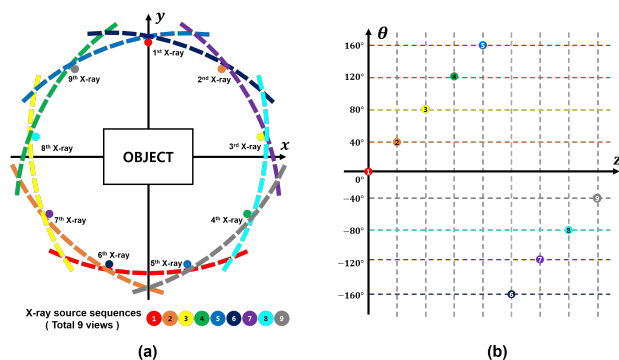


Fig. 1. X-ray source positions in our prototype 9 view dual energy CT EDS: (a)  $x - y$  direction and (b)  $\theta - z$  direction, respectively.

applications because it does not require a rotating gantry, but with only 9 projection views it is difficult to use a conventional filtered backprojection (FBP) algorithm due to severe streaking artifacts. Therefore, advanced reconstruction algorithms with fast reconstruction time are required.

For sparse-view CT EDS, model-based iterative reconstruction (MBIR) with the total variation (TV) penalty have been extensively investigated [1], [2]. Inspired by the recent success of deep learning approach for sparse view and limited angle CT [3], [4], [5], [6] that outperform the classical MBIR approach, this paper aims at developing a deep learning approach for real-world sparse view CT EDS. However, neural network training using the retrospective angular subsampling as in the existing works [3], [4], [5], [6] is not possible for our prototype system, since there are no ground-truth data for the real world sparse view CT EDS. We therefore propose a novel deep learning approach composed of image domain and sinogram domain learning that compensate for the imperfect label data.

## II. THEORY

### A. Problem Formulation

Recall that the forward model for sparse view CT EDS system can be represented by

$$g_{\theta} = \mathcal{P}_{\Theta} \mathcal{R} f \quad (1)$$

where  $\mathcal{R}$  denotes the 3D projection operator from an  $x-y-z$  volume image to a  $s-\theta-z$  domain sinogram data with  $s, \theta$  and  $z$  denoting the detector, projection angle, and the direction

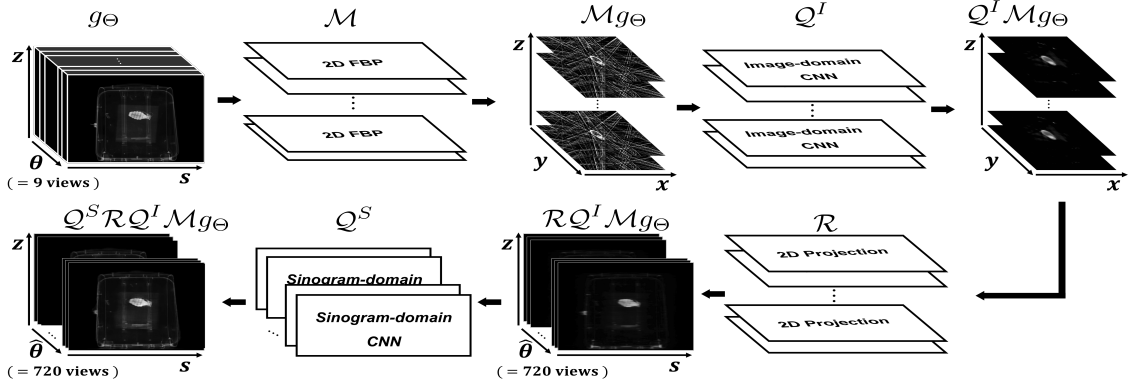


Fig. 2. Sinogram interpolation flow for the proposed method. The final reconstruction is obtained by applying the FBP for the interpolated sinogram data.

of the conveyor belt travel, respectively. See Fig. 2 for the coordinate systems. In (1),  $\mathcal{P}_\Theta$  denotes the view sampling operator for the measured angle set  $\Theta$ , and  $g_\Theta$  refers to the measured sinogram data. For each projection view data, we use the notation  $g_\theta$  and  $\mathcal{P}_\theta$ , where  $\theta$  denotes the specific view.

The main technical issue of the sparse view CT reconstruction is the non-uniqueness of the solution for (1). More specifically, there exists a null space  $\mathcal{N}_\Theta$  such that

$$\mathcal{P}_\Theta \mathcal{R} h = 0, \quad \forall h \in \mathcal{N}_\Theta,$$

which leads to infinite number of feasible solutions. To avoid the non-uniqueness of the solution, constrained form of the penalized MBIR can be formulated as :

$$\min_{f \in \mathbb{R}^3} \|\mathcal{L}f\|_1, \quad \text{subject to } g_\Theta = \mathcal{P}_\Theta \mathcal{R}, \quad (2)$$

where  $\mathcal{L}$  refers to a linear operator and  $\|\cdot\|_1$  denotes the  $l_1$  norm. For the case of the TV penalty,  $\mathcal{L}$  corresponds to the derivative. Then, the uniqueness of (2) is guaranteed that if the  $\mathcal{N}_L \cap \mathcal{N}_\Theta = \{0\}$ , where  $\mathcal{N}_L$  denotes the null space of the operator  $\mathcal{L}$ .

Instead of designing a linear operator  $\mathcal{L}$  such that the common null space of  $\mathcal{N}_\Theta$  and  $\mathcal{N}_L$  to be zero, we can design a frame  $\mathcal{W}$ , its dual  $\tilde{\mathcal{W}}$ , and shrinkage operator  $S_\lambda$  such that  $\tilde{\mathcal{W}}^\top \mathcal{W} = I$  and

$$\tilde{\mathcal{W}}^\top S_\lambda \mathcal{W}(f^* + g) = f^* \quad \forall g \in \mathcal{N}_\Theta$$

for the ground-truth image  $f^*$ . This frame-based regularization is also an active field of research for image denoising, inpainting, etc [7]. One of the most important contributions of the deep convolutional framelet theory [8] is that  $\mathcal{W}$  and  $\tilde{\mathcal{W}}^\top$  correspond to the encoder and decoder structure of a convolutional neural network (CNN), respectively, and the shrinkage operator  $S_\lambda$  emerges by controlling the number of filter channels and nonlinearities. More specifically, a convolutional neural network can be designed such that  $\mathcal{Q} = \tilde{\mathcal{W}}^\top S_\lambda \mathcal{W}$  and

$$\mathcal{Q}(f^* + h) = f^*, \quad \forall h \in \mathcal{N}_\Theta. \quad (3)$$

In other word, (3) directly removes the null space component. Eq. (3) is the constraint we use for training our neural network.

### B. Derivation of Image and Projection Domain CNNs

More specifically, our sparse view reconstruction algorithm finds the unknown  $f \in \mathbb{R}^3$  that satisfy both data fidelity and the so-called frame constraints [8]:

$$g_\Theta = \mathcal{P}_\Theta \mathcal{R} f, \quad \mathcal{Q}^I(f) = f^*, \quad (4)$$

where  $\mathcal{Q}^I$  is the image domain CNN that satisfies (3) and  $f^*$  denotes the ground-truth images that are available for training data. Now, by defining  $\mathcal{M}$  as a right-inverse of  $\mathcal{P}_\Theta \mathcal{R}$ , i.e.  $(\mathcal{P}_\Theta \mathcal{R})\mathcal{M}g_\Theta = g_\Theta, \forall g_\Theta$ , we have

$$\mathcal{M}g_\Theta = f^* + h$$

for some  $h \in \mathcal{N}_\Theta$ , since the right inverse is not unique due to the existence of the null space. Thus, we can show that  $\mathcal{M}g_\Theta$  is the feasible solution for (4), since we have

$$\mathcal{Q}^I \mathcal{M}g_\Theta = \mathcal{Q}^I(f^* + h) = f^*, \quad (5)$$

for the training data, and

$$\mathcal{P}_\Theta \mathcal{R} \mathcal{M}g_\Theta = \mathcal{P}_\Theta \mathcal{R}(f^* + h) = g_\Theta. \quad (6)$$

Therefore, the neural network training problem to satisfy (4) can be equivalently represented by

$$\min_{\mathcal{Q}^I} \sum_{i=1}^N \|f^{*(i)} - \mathcal{Q}^I \mathcal{M}g_\Theta^{(i)}\|^2 \quad (7)$$

where  $\{(f^{*(i)}, g_\Theta^{(i)})\}_{i=1}^N$  denotes the training data set composed of ground-truth image and its sparse view projection. Since a representative right inverse for the sparse view projection is the inverse Radon transform after zero padding to the missing view,  $\mathcal{M}g_\Theta^{(i)}$  in (7) can be implemented using the standard FBP algorithm. In fact, this is the main theoretical ground for the success of image domain CNN when the ground-truth data is available [3], [4], [5], [6]. Moreover, the fan-beam rebinning makes the problem separable for each  $z$  slices, so we use the 2D FBP for each slice as shown in Fig. 2.

However, the main technical difficulties in our 9-view CT EDS system is that we do not have ground-truth image  $\{f^{*(i)}\}_{i=1}^N$ . One could use physical phantoms and atomic number to form a set of ground-truth images, but those data

set may be different from the real carry-on bags, so we need a new method to account for the lack of ground-truth for neural network training. Thus, to overcome the lack of the ground-truth data, the approximate label images are generated using an MBIR with TV penalty. Then, using MBIR reconstruction as label data  $\{f^{*(i)}\}_{i=1}^N$ , a 2D image domain network  $Q^I$  is trained to learn the mapping between the artifact-corrupted 2D image and MBIR reconstruction in  $x - y$  domain.

One downside of this approach is that the network training by (7) is no more optimal, since the label data is not the ground-truth image. Thus, the generated sinogram data from the denoised 3D volume may be biased. Thus, we impose additional frame constraint to the sinogram data in addition to (4):

$$g_\theta^* = Q^S(g_\theta), \quad (8)$$

for the measured angle  $\theta$ , where  $Q^S$  is the  $s - z$  sinogram domain CNN and  $g_\theta^*$  denotes the ground-truth sinogram data measured at  $\theta$ . Then, Eq. (8) leads to the following network training:

$$\min_{Q^S} \sum_{\theta \in \Theta} \sum_{i=1}^N \|g_\theta^{*(i)} - Q^S(\mathcal{P}_\theta \mathcal{R} Q^I \mathcal{M} g_\Theta^{(i)})\|^2 \quad (9)$$

More specifically, as shown in Fig. 2, 3D sinogram data is generated in the  $s - \theta - z$  domain by applying the forward projection operator along 720-projection views after stacking the image domain network output over multiple slices to form 3D reconstruction volume in the  $x - y - z$  domain. Next, a 2D sinogram domain network  $Q^S$  is trained so that it can learn the mapping between the synthetic  $s - z$  sinogram data and the real projection data in the  $s - z$  domain. Since the real projection data is available only in 9 views, this sinogram network training is performed using synthetic and real projection data in the measured projection views. The optimization problems (7) and (9) can be solved sequentially or simultaneously, and in this paper we adopt the sequential optimization approach for simplicity.

After the neural networks  $Q^I$  and  $Q^S$  are trained, the inference can be done simply by obtaining  $x - y - z$  volume images from the 9 view projection data by slice-by-slice FBP algorithm, which are then fed into  $Q^I$  to obtain the denoised 3D volume data. Then, by applying projection operator, we generate 720 projection view data in  $s - \theta - z$  domain, which are fed into the  $Q^S$  to obtain denoised sinogram data for each  $\theta$  angle. Then, the final reconstruction is obtained by applying FBP algorithms. One could use post-processing using additional TV-based denosing. This algorithmic flow is illustrated in Fig. 2.

### III. METHODS

#### A. Real CT EDS data Acquisition

We collected CT EDS data using the prototype stationary 9 view dual energy CT-EDS system developed by GEMSS Medical Systems, Korea as shown in Fig. 1. the distance from source to detector (DSD) and the distance from source to

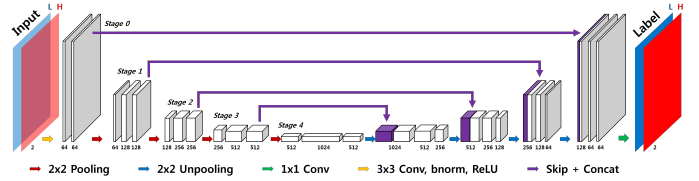


Fig. 3. CNN architecture for our image and sinogram domain networks.

object (DSO) are 1202.6mm and 648.2mm, respectively. The number of detector is 384 with a pitch of 1.5mm. The region of interest (ROI) is  $256 \times 256$  and the pixel size is  $2\text{mm}^2$ . The detectors collect low and high energy X-ray at 80KVp and 120KVp, respectively.

We collect 47 sets of projection data from the prototype CT EDS baggage scanner. Among the 47 sets, 32 dataset are simple-objects and the other set are realistic carry-on bags. The 47 set of 28 simple- and 13 baggage-objects was used during the training phase, and the validation was performed by two simple- and one baggage-object. The other set was used for test.

#### B. Network Architecture and Training

Fig. 3 illustrates modified the U-Net structure [9] for the image domain and the sinogram domain networks. To account for the multi-energy image and sinogram data, the input for the network is two channel multi-energy image and sinogram data. The proposed network consists of convolution layer, batch normalization, rectified linear unit (ReLU) [10], and contracting path connection with concatenation [9]. A detail parameters are illustrated as shown in Fig. 3.

The proposed networks were trained by stochastic gradient descent (SGD). The regularization parameter was  $\lambda = 10^{-4}$ . The learning rate has been set from  $10^{-3}$  to  $10^{-5}$ , which has been reduced step by step in each epoch. The number of epoch was 200. The batch size was 12 and the patch size for image and projection data are  $256 \times 256 \times 2$  and  $768 \times 384 \times 2$ , respectively. The network was implemented using MatConvNet toolbox (ver.24) [11] in the MATLAB 2015a environment (MathWorks, Natick). Central processing unit (CPU) and graphic processing unit (GPU) specification are i7-7700 CPU (3.60 GHz) and GTX 1080 Ti GPU, respectively.

### IV. EXPERIMENTAL RESULTS

To evaluate the performance of the proposed method, we perform image reconstruction from real 9-view CT EDS prototype system. Fig. 4 illustrates image reconstruction results of bag using various methods such as FBP, MBIR with TV penalty, image domain CNN [3], [5], and the proposed method. The FBP reconstruction results suffered from severe streaking artifacts, so it was difficult to see the threats in the tomographic reconstruction and 3D rendering. The MBIR and image domain CNN were slight better in their reconstruction quality, but the detailed 3D structures were not fully recovered and several objects were not detected as indicated by the red arrow in Fig. 4. Moreover, the 3D rendering results in Fig.

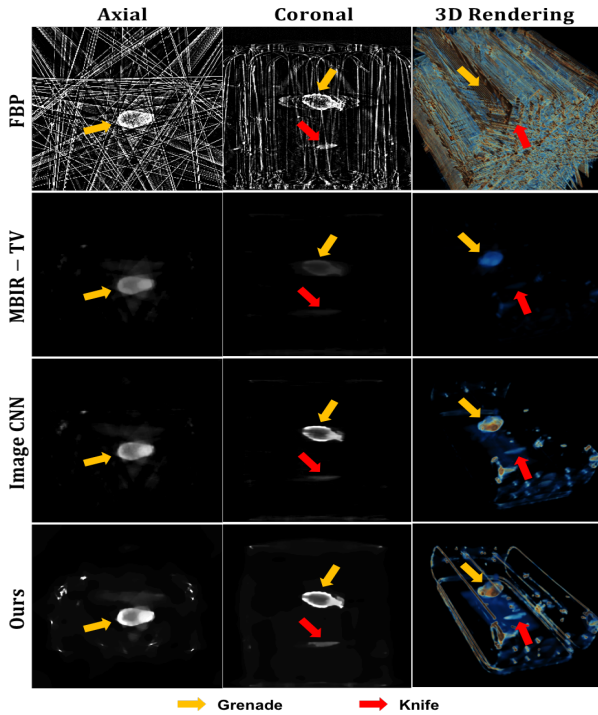


Fig. 4. Reconstruction results by various methods from 9-views CT-EDS..

4 correctly identify the shape of grenade and knife as well as the frame of the bag, which was not possible using other methods.

Because we do not have the ground-truth in the image domain, we perform quantitative evaluation using normalized mean squares error (NMSE) in the sinogram domain. More specifically, after obtaining the final reconstruction, we perform the forward projection to generate the sinogram data in the measured projection view and calculated the normalized mean square errors. Table I showed that the proposed method provides the most accurate sinogram data compared to the other methods. Moreover, the  $s - z$  projection data in Fig. 5 showed that the projection data from the proposed method is much closer to the ground-truth measurement data.

TABLE I  
NMSE VALUE COMPARISON OF VARIOUS METHODS.

Energy level	FBP	MBIR-TV	Image CNN	Ours
80 kvP	1.6647e+1	5.8247e-1	3.3207e-1	0.6845e-1
120 kvP	1.0536e+1	6.0440e-1	3.2249e-1	0.5450e-1

## V. CONCLUSION

In this paper, we proposed a novel deep learning reconstruction algorithm for a prototype 9-view dual energy CT EDS for carry-on baggage scanner. Even though the number of projection view was not sufficient for high equality 3D reconstruction, our method learns the relationships between the 2D tomographic slices in  $x - y$  domain as well as the 2D projections in  $s - z$  domain such that the artifact-corrupted image and sinogram data can be successively refined to obtain

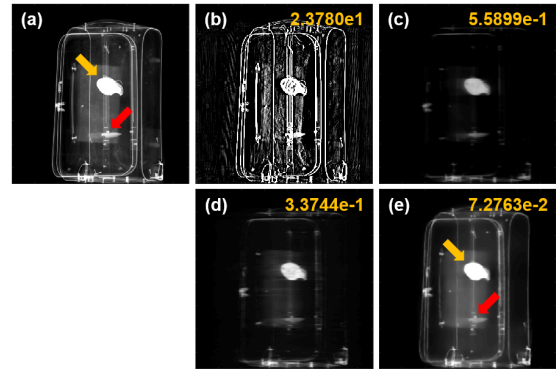


Fig. 5. A  $s - z$  domain sinogram data from (a) measurement, (b) 9-views FBP (c) MBIR, (d) image CNN, and (e) the proposed method. The number written in the images is the NMSE value. Yellow and red arrows indicate grenade and knife, respectively.

high quality images. Using real data from our prototype 9-view CT EDS system, we demonstrated that the proposed method outperforms the existing algorithms, delivering high quality three reconstruction for threat detection.

## ACKNOWLEDGMENT

This work is supported by Korea Agency for Infrastructure Technology Advancement, Grant number 17ATRP-C071164-05-000000.

## REFERENCES

- [1] Sagar Mandava, David Coccarelli, Joel A Greenberg, Michael E Gehm, Amit Ashok, and Ali Bilgin, "Image reconstruction for view-limited x-ray ct in baggage scanning," in *Anomaly Detection and Imaging with X-Rays (ADIX II)*. International Society for Optics and Photonics, 2017, vol. 10187, p. 101870F.
- [2] Sherman J Kisner, Eri Haneda, Charles A Bouman, Sondre Skatter, Mikhail Kourinny, and Simon Bedford, "Limited view angle iterative ct reconstruction," in *Computational Imaging X*, 2012, vol. 8296.
- [3] Yoseop Han, Jaejoon Yoo, and Jong Chul Ye, "Deep residual learning for compressed sensing ct reconstruction via persistent homology analysis," *arXiv preprint arXiv:1611.06391*, 2016.
- [4] Yoseob Han and Jong Chul Ye, "Framing U-net via deep convolutional framelets: Application to sparse-view CT," *arXiv preprint arXiv:1708.08333*, 2017.
- [5] Kyong Hwan Jin, Michael T McCann, Emmanuel Froustey, and Michael Unser, "Deep convolutional neural network for inverse problems in imaging," *IEEE Transactions on Image Processing*, vol. 26, no. 9, pp. 4509–4522, 2017.
- [6] Jawook Gu and Jong Chul Ye, "Multi-scale wavelet domain residual learning for limited-angle CT reconstruction," *arXiv preprint arXiv:1703.01382*, 2017.
- [7] Jian-Feng Cai, Raymond H Chan, and Zuowei Shen, "A framelet-based image inpainting algorithm," *Applied and Computational Harmonic Analysis*, vol. 24, no. 2, pp. 131–149, 2008.
- [8] Jong Chul Ye, Yo Seob Han, and Eunjoon Cha, "Deep convolutional framelets: A general deep learning framework for inverse problems," *arXiv preprint arXiv:1707.00372*, 2017.
- [9] Olaf Ronneberger, Philipp Fischer, and Thomas Brox, "U-net: Convolutional networks for biomedical image segmentation," in *International Conference on Medical Image Computing and Computer-Assisted Intervention*. Springer, 2015, pp. 234–241.
- [10] Alex Krizhevsky, Ilya Sutskever, and Geoffrey E Hinton, "Imagenet classification with deep convolutional neural networks," in *Advances in neural information processing systems*, 2012, pp. 1097–1105.
- [11] Andrea Vedaldi and Karel Lenc, "Matconvnet: Convolutional neural networks for matlab," in *Proceedings of the 23rd ACM international conference on Multimedia*. ACM, 2015, pp. 689–692.